nature communications

Article | Article in Press

https://doi.org/10.1038/s41467-026-79126-z

Global arable land redistribution toward the tropics and drylands under human settlement expansion

Received: 2 September 2026

Accepted: 13 October 2026

Published online: 29 October 2026

Check for updates

Lun Gao[1,2] ✉, Xiaoman Lu[2], Weston Anderson[3,4,5], Corey Lesk[6,7,8], Elise Mazur[9], Fred Stolle[9], Peter Potapov[9], Francesco N. Tubiello[10], Steffen Fritz[11], Jiafu Mao[2], Liangzhi You[12,13] & Deepak Ray[1]

Arable land extent has undergone widespread changes across many regions worldwide through processes such as urban encroachment, forest conversion to agriculture, and dryland farming expansion. Yet an integrated understanding of global arable land dynamics remains limited. Using our self-developed arable land product integrated with global human settlement layers, Köppen–Geiger climate classifications, and historical land-use reconstructions, we show that the disproportionate climatic co-location of arable land and human settlements fundamentally structures global arable land dynamics. Across much of the climatically favorable Northern Hemisphere, earlier co-development of settlements and agriculture has increasingly shifted toward competition, with settlement expansion displacing cultivation from temperate regions and contributing to its expansion into adjacent arid zones. In contrast, low-latitude tropical regions continue to expand both systems at the expense of natural landscapes, partly driven by agricultural investment from Northern Hemisphere. Globally, these contrasting trajectories reveal a broader redistribution of agricultural pressure from climatically favorable regions toward less-exploited tropical and arid environments, linking settlement expansion and agricultural displacement to diverse environmental consequences including deforestation, biodiversity loss, groundwater depletion, and vegetation greening. These findings highlight the need to consider both local settlement–agriculture competition and broader agricultural redistribution when planning future food production and settlement growth.

Driven by humanity's demand for food, fiber, fuel, and shelter, approximately three-quarters of the planet's terrestrial surface has already been altered over the past millennium[1–3]. Arable land, though occupying slightly more than 10% of Earth's ice-free surface[4], remains the primary source of food commodities sustaining over 8 billion people. With the global population projected to approach 10 billion by 2050 and living standards rising worldwide[5], pressures to expand crop production are mounting[6–12]. Such agricultural expansion has been extensively documented in tropical forest regions[13–18] and is increasingly extending into arid regions where cultivation often depends on intensive groundwater extraction[19–21]. At the same time, human settlement expansion is accelerating, leading to the loss of productive arable land in many regions of the world[22–24]. By 2050, an additional 2.5 billion people—approximately 70% of the global population—are expected to reside in urban areas[5,25], further intensifying competition between settlement and agricultural land. This simultaneous

A full list of affiliations appears at the end of the paper. ✉e-mail: gaoxx996@umn.edu

expansion and displacement of arable land can generate environmental consequences far beyond food security, with implications for deforestation, water resources, biodiversity, greenhouse gas emissions, climate change, wildfire, and conservation policies[1,13–24,26–29]. However, how these distinct patterns of arable land dynamics are connected at the global scale remains unclear.

To advance the understanding of global arable land dynamics, we hypothesize that arable land and human settlements are preferentially concentrated within similar favorable climatic regimes because both agricultural productivity and long-term settlement development are constrained by temperature and water availability. This shared climatic dependence can lead to a disproportionate concentration of both systems within climatically favorable regions. As development intensifies, however, settlement expansion within these regions may increasingly compete with existing arable land for space, potentially contributing to the redistribution of agricultural land toward less intensively developed climatic regions. To test this hypothesis, we pose three key questions: (1) Is the climate-constrained spatial correlation between arable land and built-up land observable on a global scale? (2) What are the global patterns of arable land dynamics in response to human settlement expansion? (3) How is arable land redistributed across different climate regimes under human settlement expansion?

To answer these questions, we generated 1-km Global Arable Land Fraction (GALF) maps for 2000, 2010, and 2020 by integrating five land cover products and FAO country-level statistics, considering that strong agreement among products enhances confidence in arable land detection (Methods). Following FAO's land use definition[30], arable land is defined as the sum of areas under temporary crops, temporary meadows and pastures, and temporary fallow. In essence, it describes the various typologies for cultivating annual crops around the world while maintaining soil productivity through rotation cycles of up to 5 years that may include crops, pastures, or fallow, depending on management intensity[31]. The FAO cropland class is obtained by adding arable land to permanent woody crops (e.g., oil palm, rubber, and cocoa) that were not considered, given the scope of this paper. Concurrent human settlement development was captured using the 1-km Global Human Settlement Layer (GHSL) built-up fraction[32], where built-up areas are defined as the gross building footprint enclosed by the outer building walls, including both dense urban cores and low-density rural settlements while excluding impervious surfaces such as roads. Climate zones were delineated using the 1-km Köppen–Geiger climate classification[33]. Additionally, historical land cover dynamics were examined using 5-arcminute HYDE3.4 (0-2024) data[34]. Further details on all datasets and processing procedures are provided in the "Methods."

Results

Climate structuring of arable land and human settlements

By comparing maps of arable land and built-up areas, we show that the two land-use types are highly coupled and spatially structured by climate, with both disproportionately concentrated within similar climatic regions (Fig. 1a–c). As of 2020, 90% of the world's arable land and 84% of built-up areas were concentrated within just ten of the thirty Köppen–Geiger climate classes, spanning mildly cold (Dfb, Dfa, Dwa), temperate (Cfa, Cwa, Cfb), arid steppe (BSk, BSh), tropical savannah (Aw), and arid desert (BWh). While arable land and built-up areas are present in some parts of the tropical and arid zones, tropical rainforest (Af), tropical monsoon climates (Am), arid desert (BWh), and hyper-arid deserts (BWk) typically function as a natural boundary limiting large-scale arable land and human settlement development. A finer-scale examination of northwestern Canada (Fig. 1a1–c1) illustrates how the Dfb climate zone sharply limits arable land and built-up expansion, with similar constraints observed at agricultural frontiers across other continents (Fig. 1b1–c5). These climatic constraints and the uneven distribution of climate zones create pronounced global disparities in land-use intensity. Arable land and built-up densities are markedly higher in North America, Europe, East Asia, and South Asia, but relatively lower elsewhere (Fig. 1a, b).

Consequently, aggregating arable land and built-up areas by Köppen–Geiger climate zones within each continent reveals strong positive correlations at both continental and global scales, consistent with a disproportionate concentration of both systems within particular climatic regimes (Fig. 1d and Supplementary Table S1). Specifically, except Oceania—where the correlation is not statistically significant, likely due to the relatively limited extent of arable land and built-up areas—correlation coefficients consistently exceed 0.76 ($p < 0.01$) across all continents. The strongest correlations occur in South Asia ($R = 0.99$), Africa ($R = 0.98$), and South America ($R = 0.98$). By contrast, other continents typically exhibit more moderate values ($R = 0.76$–0.86), accompanied by notable decreases in arable land within the climate zone containing the largest built-up areas. This disparity is likely attributable to the relatively limited emergence of large-scale competition between arable land and built-up areas in the former regions (as discussed below).

Human settlement expansion driving transformational paradigms of arable land dynamics

Despite the strong spatial correlation between arable land and built-up systems, the extent to which human settlement growth directly drives arable land dynamics remains unclear. To further test our hypothesis and assess potential causality, we examined the global dynamics of arable land in relation to built-up expansion. Figure 2a demonstrates the difference in GALF between 2020 and 2000, alongside concurrent built-up changes at 0.05° resolution, derived from 1-km original maps. Globally, 67% of built-up expansion occurred within 1 km of existing or recently lost arable land, and 40% coincided with declines in arable land (Fig. 2b). The remaining expansion mainly took place in previously uncultivated landscapes along the margins of arable land or within areas surrounded by it, such as in eastern Brazil and the Appalachian Mountain region in the United States. This unbalanced pattern of built-up expansion has led to substantial arable land loss across Northern Hemisphere regions with relatively developed human settlements, including eastern North America, central Europe, mainland East Asia, northern South Asia, and the Southeast Asian peninsula. Consistent with previous research[22], we observed that the indirect impacts of built-up expansion on arable land displacement extended far beyond its direct effects, with nearly 9 km^2 of arable land loss associated with each 1 km^2 of built-up expansion in competition regions (Supplementary Table S2). This is likely because human settlement development not only directly encroaches on nearby arable land but also drives rural outmigration, thereby accelerating rural land abandonment[35,36]. Together, these dynamics enable meaningful comparison of net changes in arable land and built-up areas at climatic or continental scales, despite the fact that total built-up areas remain much smaller than arable land globally (Fig. 1). For example, net increases in built-up areas have already exceeded net decreases in arable land across Europe-North Asia and East Asia (Supplementary Table S2).

On continental scales—specifically in North America, the Eurasian Agricultural Belt (i.e., the heavily cultivated regions of the Eurasian Steppe), East Asia, and South Asia, which are characterized by extensive arable land interspersed with large areas of natural landscapes—a distinct spatial gradient emerged, with arable land increasingly displaced from densely human settlement cores toward relatively less developed peripheral areas (Fig. 2a). This pattern becomes more pronounced when a zero threshold is used instead of ±2% to classify increases, decreases, and stability in arable land and built-up areas (Supplementary Fig. S2). Taking North America as an example, built-up areas expanded markedly from the southeast towards the northwest,

https://doi.org/10.1038/s41467-026-79126-z

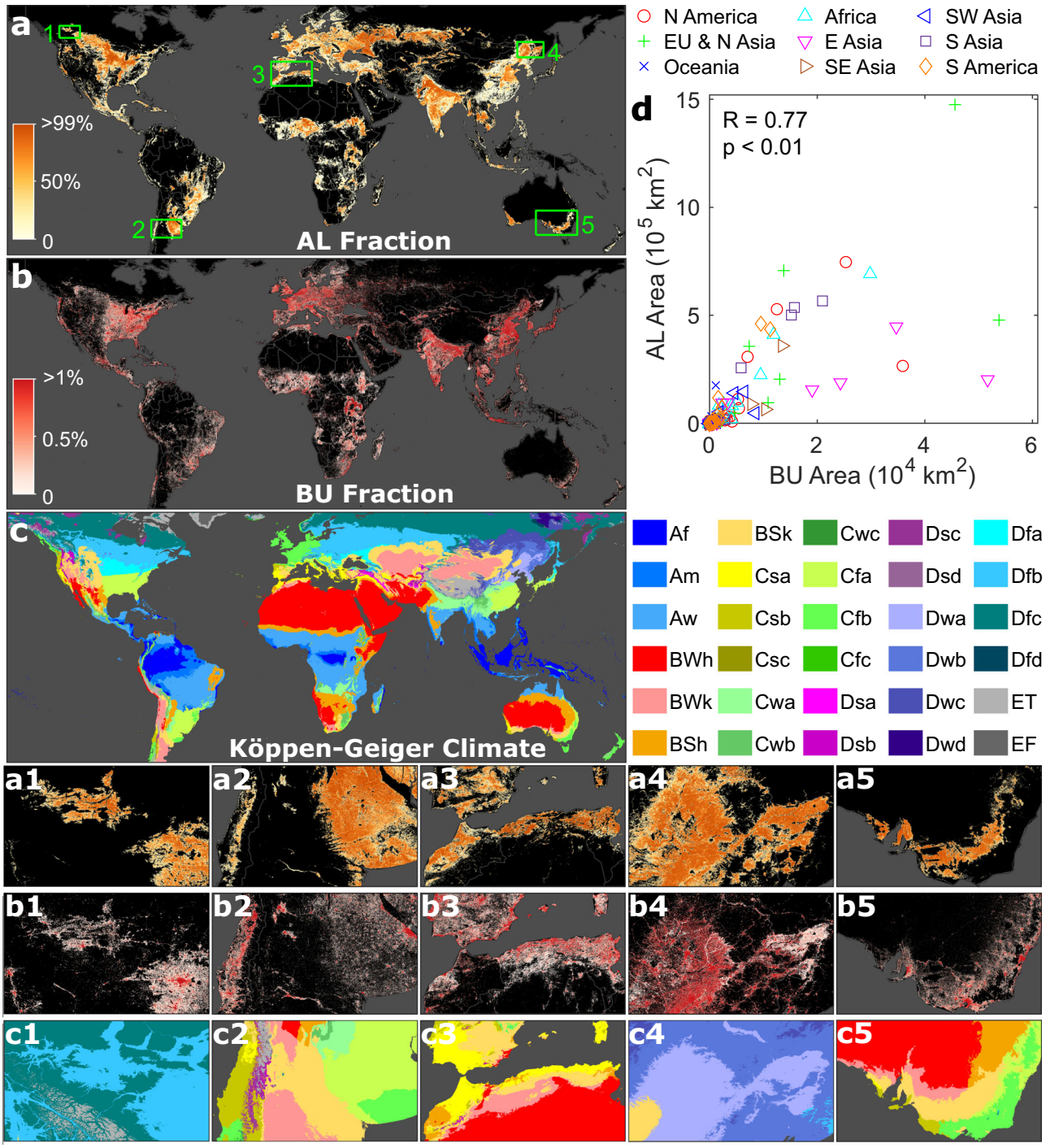


Fig. 1 | Arable land (AL) and built-up (BU) areas are strongly structured by climate. a–c Global maps of AL fraction, BU fraction, and Köppen–Geiger climate zones at 0.05° for 2020. Climate type specifications are provided in the "Methods." **d** Relationship between AL and BU areas across continental-scale Köppen–Geiger climate zones. Corresponding continental-scale correlation coefficients are reported in Supplementary Table S1. Regional zoom-ins showing AL fraction (**a1**–**a5**), BU fraction (**b1**–**b5**), and climate zones (**c1**–**c5**) at 1 km in northwestern Canada (52.0–57.6° N, 123–112° W), Argentina–Chile (40.15–32.0° S, 74–58° W), North Africa (29.9–41.0° N, 10.15° W–11.6° E), northeastern China (43.0–50.15° N, 121–135° E), and southeastern Australia (39.0–27.75° S, 131–153° E), respectively. Consistent patterns are observed when replicating the figure using the Global Land Analysis and Discovery (GLAD) data[64] (Supplementary Discussion and Fig. S1). BU data are derived from the Global Human Settlement Layer (GHSL)[32,92], and Köppen–Geiger climate classification data are from Beck et al.[33]. Both datasets are licensed under CC BY 4.0 (https://creativecommons.org/licenses/by/4.0/legalcode.en) and were processed for visualization.

accompanied by widespread arable land decline in the southeastern region. Meanwhile, arable land across the central Corn Belt (e.g., Indiana, Illinois, and Iowa) remained largely stable despite substantial built-up expansion, suggesting that a preliminary stage of competition between the two systems has already emerged. By contrast, at the agricultural frontiers of the Midwest, we observed extensive arable land expansion in natural lands experiencing minimal built-up growth, primarily at the expense of grasslands and wetlands[37]. Similar spatial gradients were evident along the Eurasian Agricultural Belt (west to east), across China (southeast to northwest), and within India (northern and coastal regions to central forested areas), reflecting consistent patterns of arable land displacement under expanding human

https://doi.org/10.1038/s41467-026-79126-z

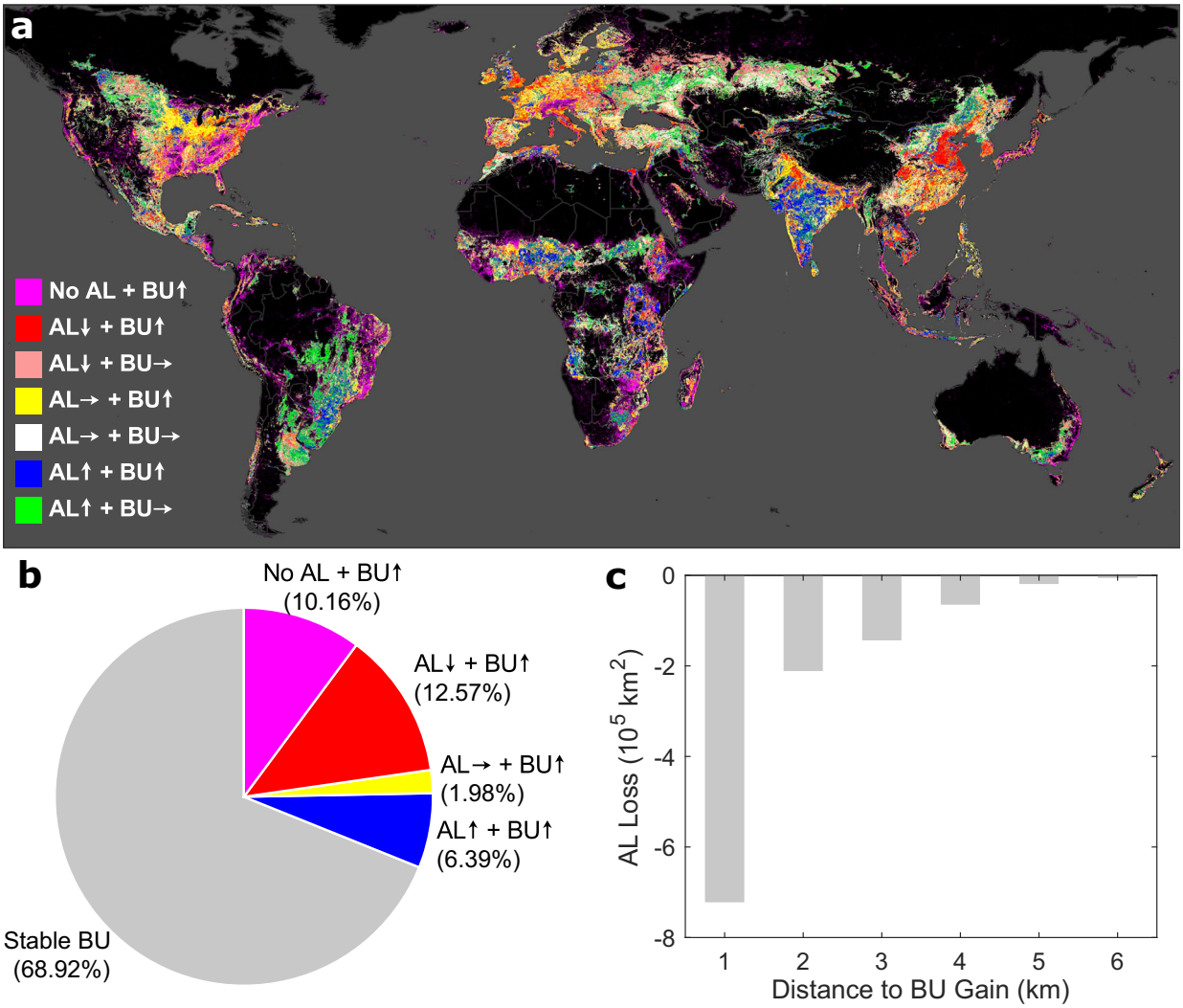


Fig. 2 | Dynamics of arable land (AL) in relation to built-up (BU) area between 2020 and 2000. a Spatial distribution of GALF changes with and without concurrent BU expansion at 0.05°, derived from 1-km original maps. Areas with changes >2%, <−2%, and between these thresholds were classified as increase ("↑"), decrease ("↓"), and stable ("→"), respectively. A zero-threshold classification was also tested (Supplementary Fig. S2). For clarity, each category is shown individually (Supplementary Fig. S3), with the corresponding area statistics of AL and BU for each category reported in Supplementary Table S2. **b** Proportion of BU expansion associated with AL dynamics from 2000 to 2020, where stable BU equals the total BU area in 2000. **c** AL losses ranked by distance to the nearest BU gain during 2020 and 2000, using buffers around pixels with increased BU area at 1 km. A 0-pixel buffer (i.e., distance = 1 km) represents concurrent AL loss and BU gain within the same pixel. Distances up to 6 km were considered, covering 99.8% of AL loss. Consistent patterns are observed when replicating the figure using the GLAD data[64] (Supplementary Discussion and Fig. S4). BU data are derived from the Global Human Settlement Layer (GHSL)[32,92], licensed under CC BY 4.0 (https://creativecommons.org/licenses/by/4.0/); the data were processed for analysis and visualization.

settlements. In Southeast Asia, where the terrain is highly fragmented, widespread arable land displacement accompanied built-up expansion across the Southeast Asian peninsula and Indonesia, whereas arable land expanded substantially in Myanmar (Fig. 2a and Supplementary Table S2).

Further analysis showed that arable land loss is highly concentrated near expanding human settlements. Specifically, 62% of the global arable land loss happened within 1 km of built-up area gain, rising to 99.8% within 6 km (Fig. 2c). Notably, total arable land loss declined sharply with increasing distance from built-up area gain—by more than 30% for each additional kilometer. Note that arable land decline also occurred at the frontiers of expansion with relatively limited built-up growth, such as western Russia, central China, and southern Saskatchewan in Canada (Fig. 2a and Supplementary Fig. S3). These declines were driven by factors beyond human settlement development, including post-Soviet land-use transitions from state-controlled to market-driven agricultural systems[38], China's large-scale reforestation programs[39], land degradation in marginal cultivation zones[40], and climate adaptation[41,42]. Together, these findings suggest that for regions located away from densely populated areas and characterized by sufficient natural landscapes, broader socioeconomic and environmental factors become increasingly important in shaping the allocation of arable land. This pattern complements our hypothesis, where human settlement expansion primarily drives the outward displacement of arable land into surrounding natural landscapes and climatic regimes, while the subsequent allocation within these regions is governed by broader socioeconomic and environmental drivers.

In contrast to regions in the Northern Hemisphere, both arable land and built-up areas expanded extensively across South America, Africa, and Oceania; however, built-up expansion rarely encroached on arable land, occurring mainly in adjacent areas or alongside arable land expansion. Only about 20% of built-up expansion was associated with arable land loss, primarily in northern, eastern, and central Africa, as well as in Ecuador and southern Brazil. This is attributed to the

https://doi.org/10.1038/s41467-026-79126-z

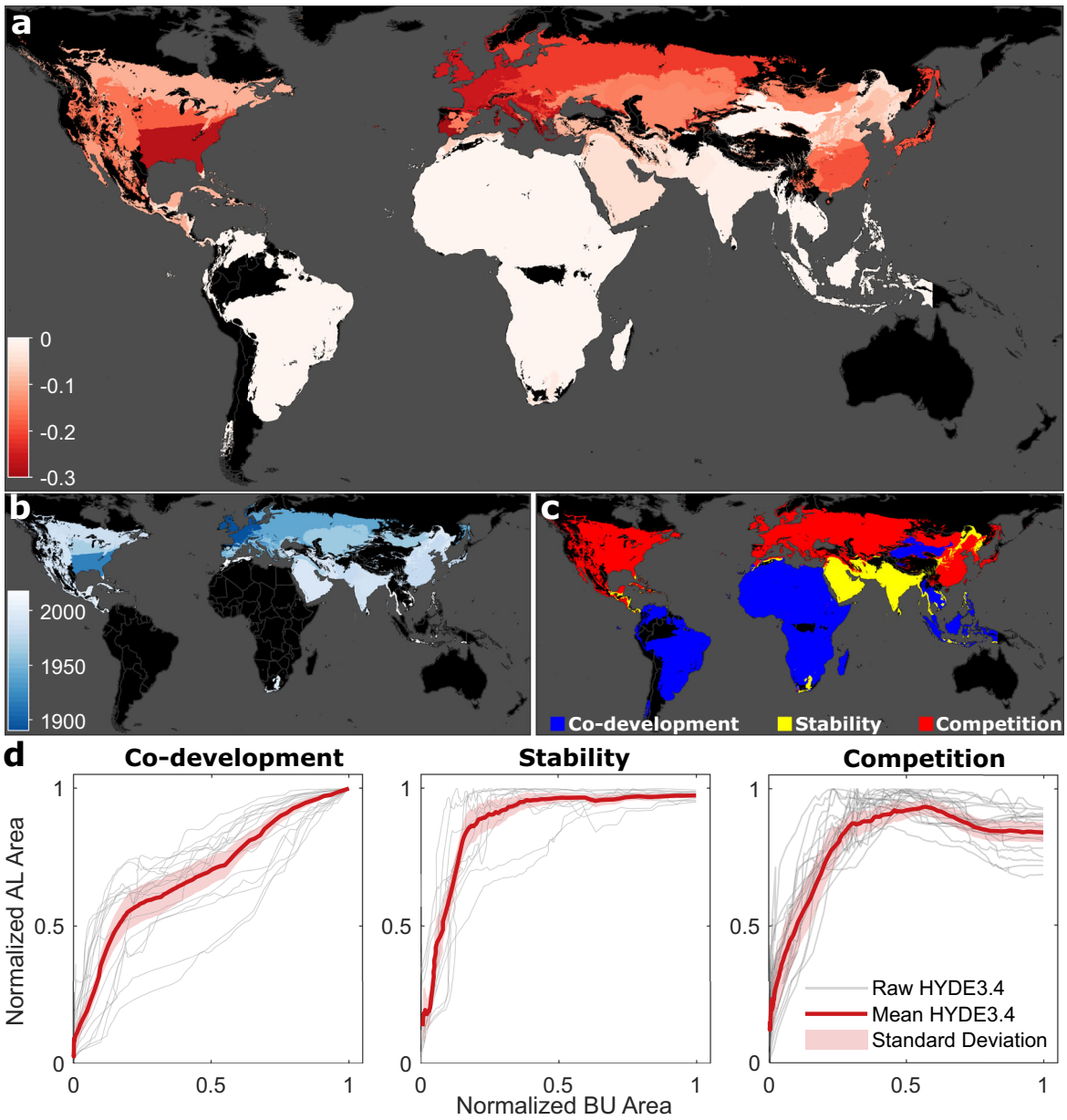


Fig. 3 | Recent trends of arable land (AL) and paradigms of change in AL and built-up (BU) area. a Recent trends in total AL across Köppen–Geiger climate zones on each continent based on HYDE3.4 data (0-2024). Trends are defined as the ratio of AL in 2024 to its historical maximum. Only climate zones with AL > 10,000 km^2 and BU > 1000 km^2 were included. **b** Year of historical maximum AL for regions exhibiting a downward trend in AL, indicating the onset of subsequent decline. **c**, **d** Co-development, stability, and competition regions and paradigms denoted by AL gain, stability, and loss under concurrent BU increase across continental-scale climate zones. AL gain, stability, and loss are defined as cases where the 2024 AL area is at its historical maximum, within 5% of the maximum, or more than 5% below it, respectively. For consistency, both AL and BU were normalized by their respective maximum values. The raw HYDE3.4 time series of AL and BU are shown in Supplementary Fig. S5. When replicating the figure using the LUH2 data[101], consistent patterns are observed (Supplementary Discussion and Fig. S6). Köppen–Geiger climate classification data are from Beck et al.[33], licensed under CC BY 4.0 (https://creativecommons.org/licenses/by/4.0/); the data were processed for analysis.

abundance of natural landscapes in these continents, which enables human settlement and agricultural expansion to proceed largely independently without direct competition for land.

To further understand the formation of diverse patterns of arable land change, we analyzed the evolution of historical arable land and built-up areas across continental-scale Köppen–Geiger climate zones using HYDE3.4 data, which reconstruct historical land covers from census data, archeological records, and satellite observations (Methods). This analysis was performed because HYDE3.4 offers a long-term perspective on land-use dynamics by extending back to 0 CE, albeit with a less precise definition of arable land. Largely consistent with the GALF-derived results, Fig. 3a shows that much of the Northern Hemisphere is undergoing a decline in arable land relative to its historical peak, while built-up areas have expanded exponentially throughout the late modern and contemporary periods (Supplementary Fig. S5). Specifically, significant proportional declines in arable land were observed in mainland Europe (−31 to −25%) and the eastern United States (−27 to −18%), followed by eastern Europe (−22%) and eastern China (−19 to −17%). Notably, the four most affected climate regimes are exclusively temperate. The onset of these declines varies chronologically (Fig. 3b), occurring first in mainland Europe circa 1890, followed by the United States around 1920, and more recently in China

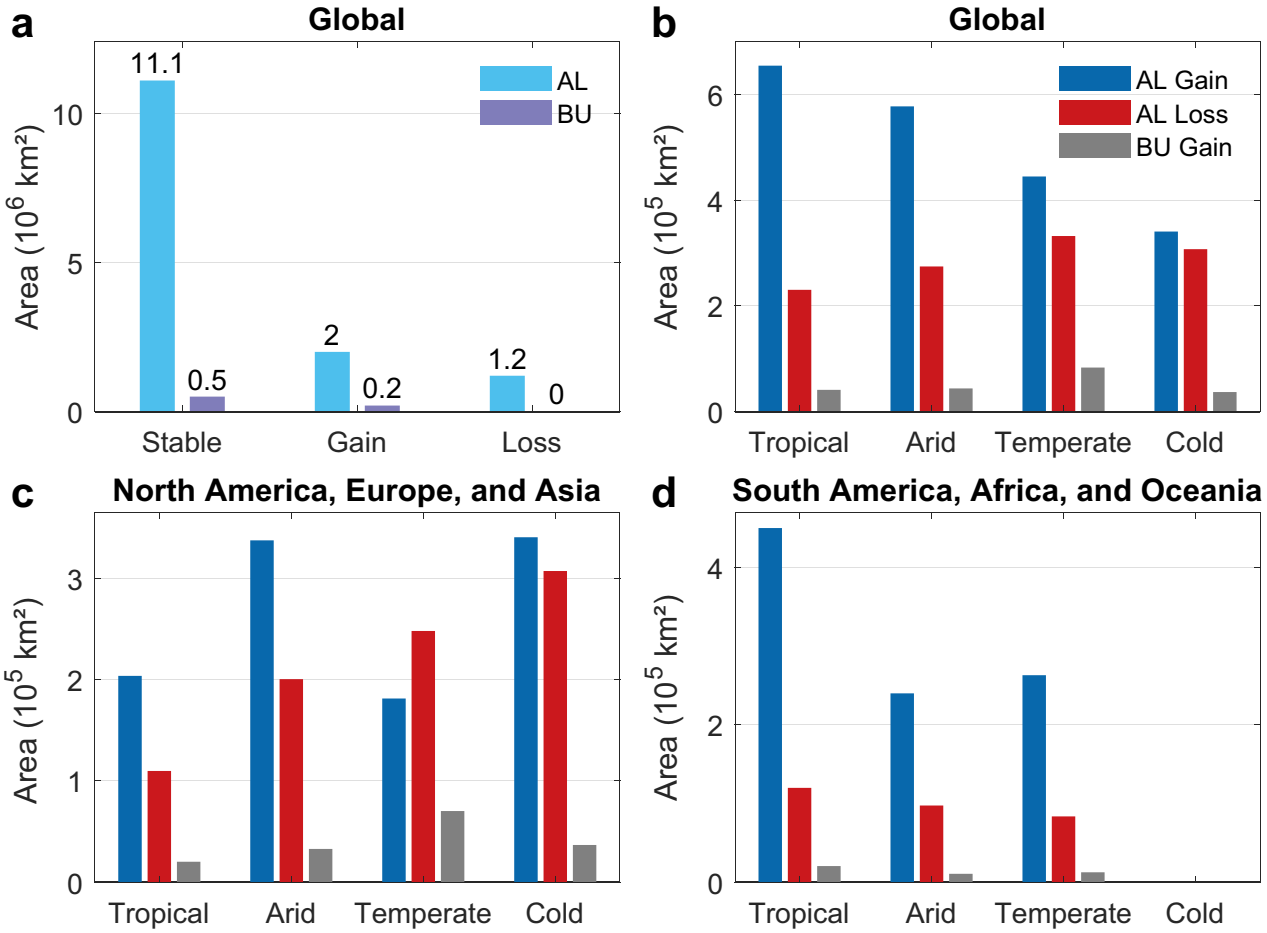


Fig. 4 | Global arable land redistributed toward tropical and arid climates between 2000 and 2020. a Global totals of stable, gained, and lost arable land (AL) and built-up (BU) areas from 2000 to 2020. **b**–**d** Changes in AL and BU areas aggregated globally and by region, distinguishing areas of extensive displacement (North America, Europe, and Asia) and expansion (South America, Africa, and Oceania) across the four major Köppen–Geiger climate zones. Similar patterns are observed when replicating the figure using the GLAD data[64] (Supplementary Discussion and Fig. S7). BU data are derived from the Global Human Settlement Layer (GHSL)[32,92], and Köppen–Geiger climate classification data are from Beck et al.[33]. Both datasets are licensed under CC BY 4.0 (https://creativecommons.org/licenses/by/4.0/legalcode.en) and were processed for analysis.

around 1979. By contrast, low-latitude regions and the Southern Hemisphere continue to support concurrent expansion of both arable land and built-up areas (Fig. 3a, b).

Their coupled trajectories fall into three paradigms of land-use change (Fig. 3c, d): *co-development*, where arable land expands alongside human settlement growth (South America, Africa, Southeast Asia, and Northwest China); *stability*, where arable land plateaus despite continued human settlement development (South Asia, Southwest Asia, and Northeast China); and *competition*, where arable land declines as human settlements continue to expand following earlier stages of co-development and/or stability (North America, Europe, Central Asia, and East Asia). These trajectories—from coexistence to competition—support our hypothesis, suggesting that regions currently in early co-development phases may evolve toward competition as human settlement intensifies.

Global arable land redistribution toward tropics and drylands

In the context of arable land encroachment driven by the expansion of human settlements, identifying global patterns of spatial change in arable land is essential for developing adaptive management strategies. Figure 4 evaluates the dynamics of arable land and built-up areas across four dominant Köppen–Geiger climate zones during 2000–2020. During this period, global arable land increased by 7% from 12.3 to 13.1 million km², with 11.1 million km² remaining stable, 2.0 million km² newly cultivated, and 1.2 million km² lost (Fig. 4a). In contrast, global built-up area surged by 45% from 0.46 to 0.66 million km², with no losses detected. Although the total built-up area remains much smaller than arable land (~20:1 in 2020), the magnitude of net arable land gains relative to built-up expansion is more comparable, with a ratio of ~4:1. Further global analysis reveals that 83% of net arable land gains were concentrated in tropical and arid zones, whereas losses were slightly more prevalent in temperate and cold climates than in other regions (Fig. 4b). In comparison, 41% of built-up expansion occurred in the temperate climates, followed by arid (21%), tropical (20%), and cold (18%) climates. Consequently, the ratios of net arable land gains to built-up expansion decrease markedly from tropical (10.3) and arid (6.9) climates to temperate (1.4) and cold (0.9) climates.

When comparing regions characterized by arable land displacement (North America, Europe, and Asia) with those of expansion (South America, Africa, and Oceania), pronounced differences emerge. In regions experiencing displacement (Fig. 4c), net arable land losses (6.7×10^4 km²) occurred primarily in temperate climates and were outpaced by built-up expansion (7.0×10^4 km²), highlighting direct human settlement expansion pressure on farming systems. By contrast, about 69% of net gains were concentrated in arid zones, suggesting a compensatory redistribution toward marginal and water-limited climates. This pattern is evident in countries like China, the United States, and India (Fig. 2a). In China, the displacement of prime

arable land by rapid human settlement growth in coastal and central provinces[23,24]—combined with farmland protection measures such as the Basic Farmland Protection Regulation and the "red line" policy safeguarding ~1.2 million km^2 of arable land—has pushed cultivation into the semi-arid northwest[43]. In the United States, farm subsidy programs[44] encouraged arable land expansion into marginal and environmentally sensitive drylands of the Great Plains, partly offsetting arable land losses to human settlement growth in fertile regions like the Corn Belt. In India, the Indira Gandhi Canal enhanced water availability from the early 2000s, driving substantial arable land and human settlement growth in the Thar Desert[21], thereby alleviating pressure for arable land expansion in more densely settled regions.

On the other hand, in regions dominated by rapid arable land expansion (Fig. 4d), arable land increased substantially across tropical, arid, and temperate zones, with the largest net gains (51%) observed in tropical climates, followed by temperate (27%) and arid (22%) climates. Across these zones, the ratios of net arable land gains to built-up expansion consistently exceeded 13:1, indicating negligible competition between the two. This pattern reflects that arable land expansion primarily occurred at the expense of natural ecosystems[16].

Discussion

Overall, the results support our hypothesis and show the redistribution of global arable land toward the tropics and drylands. We find that arable land and built-up land are spatially correlated and disproportionately concentrated within similar climate types (Fig. 1). This climatic structuring contributes to pronounced disparities in land-use intensity worldwide, with markedly higher arable land and built-up densities in North America, Europe, East Asia, South Asia, and Southeast Asia, and substantially lower densities elsewhere. Consequently, human settlement expansion has emerged as a key driver of arable land redistribution on these continents (Figs. 2 and 3). In contrast, in South America, Africa, and Oceania, arable land and built-up areas continue to expand, with minimal arable land displacement, primarily at the expense of natural landscapes. Moreover, the coupled evolution of arable land and built-up areas are summarized into three paradigms: *co-development*, characterized by the simultaneous expansion of both land types; *stability*, in which arable land remains relatively constant despite ongoing human settlement growth; and *competition*, marked by a decline in arable land as human settlements expand following an earlier period of *co-development* or *stability* (Fig. 3). Lastly, we find that global arable land is redistributed from historically favorable temperate climates—where the magnitudes of net arable land change and built-up expansion have become comparable despite the much larger total extent of arable land—toward more marginally tropical and arid regions (Fig. 4). Notably, expansion in arid zones is more closely associated with extensive arable land displacement, whereas expansion in tropical zones is mainly concentrated in regions experiencing both arable land and human settlement growth.

While these results are broadly consistent with previous land-use change studies, our proposed hypothesis provides a unifying framework by connecting the three land-use paradigms identified above—*co-development*, *stability*, and *competition*—with subsequent agricultural redistribution across climatic regions. Specifically, prolonged co-development or stability can transition into competition as human settlements expand into existing arable land, while the associated loss of arable land in densely developed regions may contribute to a broader redistribution of agricultural pressure toward tropical, dryland, and other resource-constrained environments. Studies suggest that more than half of newly expanded urban land by the 2040 s will occur on existing arable land[23,24], which can trigger indirect land-use change, including deforestation, through arable land displacement[22]. At the same time, cropland expansion pressure, including woody permanent crops, has been predominantly concentrated in the tropics[18], where more than 90% of tropical deforestation between 2011 and 2015 was driven by agricultural expansion[17]. This pattern is further supported by documented forest loss associated with agricultural encroachment in Southeast Asia[14,15] and large-scale soybean expansion in South America[16]. Meanwhile, arid regions such as the Thar Desert in northwestern South Asia have experienced rapid urban and agricultural expansion, with mean annual greenness increasing by 38% between 2001 and 2023[21]. Such dryland agricultural expansion is often sustained by intensive groundwater withdrawals[19–21]. In addition, our results are consistent with the observed expansion of cropland, including woody crops, into highland areas[14,45], where elevation is a key determinant of regional climate conditions[46]. Together, these examples illustrate how human-settlement expansion, agricultural displacement, and subsequent redistribution can unfold differently across tropical, dryland, and highland environments. Overall, these findings are consistent with our hypothesis that human-settlement-driven arable land loss in densely developed regions is linked to a broader redistribution of agricultural pressure toward tropical, dryland, and resource-constrained natural environments.

Our findings further align with the phenomenon of global arable land leakage in an increasingly interconnected world, where globalization—through commodity trade, capital investment, labor mobility, transport, and logistics networks—spatially separates agricultural production from final consumption and redistributes land-use pressures across national and regional boundaries[47–49]. By 2005, about 16% of global arable land requirements for food were supplied through international trade[50]. For example, although South America experienced a striking expansion of agricultural land, its own arable land requirements for food did not increase substantially after 1980[50]. This pattern is further reinforced by the expansion of U.S. agribusinesses into Argentina, Brazil, and Paraguay for soybean production[51], alongside China's arable land protection policies that have driven large-scale soybean imports from South America[16] and stimulated agricultural investments in Southeast Asia and Africa[52]. Likewise, Gulf countries such as Saudi Arabia, UAE, and Qatar have leased or purchased farmland in Sudan, Ethiopia, and other African nations to secure food supplies, effectively outsourcing agricultural land demand[52]. While these studies highlight the importance of global economic dynamics in driving arable land expansion in developing regions at the expense of natural areas, they do not account for arable land displacement by human settlement expansion (Fig. 2), the historical co-evolution of arable land and built-up areas (Fig. 3), and the redistribution of arable land toward drylands within developed regions (Fig. 4c). To this end, we argue that, beyond the regional redistribution of agricultural pressure into adjacent natural landscapes, global arable land leakage represents another specific manifestation of cross-border transfer of agricultural pressure under our proposed framework, linking telecoupled economic processes with spatially explicit land-use dynamics.

Our findings also contribute to broader debates on agricultural land abandonment[35,36], land-use intensification[53–55], and land sparing versus land sharing for biodiversity conservation[56,57]. These processes are often interpreted within individual regions, yet their consequences may extend beyond the landscapes in which they occur. Recent global syntheses show that agricultural intensity, biodiversity, food security, population density, governance, and remoteness form distinct regional social–ecological configurations, implying that no single land-use strategy is universally appropriate[58]. Rather, conservation, restoration, and ecological intensification need to be tailored to regional conditions. Within this context, our results add a dynamic spatial dimension by showing how local trajectories of settlement–agriculture interactions are connected to the broader redistribution of agricultural pressure. Agricultural abandonment or intensification in densely developed regions may reduce local pressure on land, but such apparent land sparing does not necessarily translate into global land sparing if agricultural demand is displaced toward tropical, arid, or other environmentally sensitive regions. Conversely, continued

agricultural expansion in these receiving regions can impose substantial costs on biodiversity[56,57], forests[14–18], and water resources[19–21]. Our framework therefore extends the land sparing–land sharing debate beyond local land allocation to consider where agricultural pressure is ultimately redistributed, highlighting the need to evaluate land-use strategies within a telecoupled global system.

Our findings also provide a broader context for considering how arable land dynamics intersect with land-use policy. In regions where we observe widespread arable land displacement, including North America, Europe, and Asia, a range of policies have been introduced to protect agricultural land or maintain its productive capacity[59,60]. Examples include the Farmland Protection Policy Act in the United States, the Common Agricultural Policy in the EU, and China's Permanent Basic Farmland Protection and "red line" policies. Although our analysis does not directly evaluate the effectiveness of these policies, their prevalence in regions experiencing strong competition between arable land and human settlements highlights growing policy attention to farmland preservation. In tropical regions, where our results show continued expansion of arable land, policy efforts have instead often emphasized forest conservation[61], including Brazil's Forest Code, REDD+ initiatives, and Indonesia's restrictions on primary forest and peatland conversion. Nevertheless, agricultural expansion remains an important driver of tropical forest loss. Recent evidence further shows that even policies effective in reducing deforestation may not address other forms of forest degradation[61], emphasizing the need for more integrated land-management approaches. In dryland regions, where we observe continued arable land expansion, groundwater extraction is likewise subject to a range of regulatory frameworks. Examples include China's Regulation on Groundwater Management, the EU's Groundwater Directive, India's Model Groundwater (Sustainable Management) Bill, Australia's Sustainable Diversion Limits, and Mexico's National Water Law. Yet rapid groundwater declines remain widespread in many intensively cultivated drylands[19,20]. Together, these patterns suggest that agricultural expansion, settlement growth, forest conservation, and water management are often addressed through separate policy frameworks, whereas their interactions may warrant more integrated land-use planning.

While our hypothesis offers a unifying framework linking human settlement expansion, climate-scale arable land redistribution, tropical deforestation, dryland greening, global arable land leakage, rural land abandonment, land-use intensification, the ongoing land sparing–land sharing debate, and land-use policy, several limitations in our data and interpretation must be acknowledged. First, the generated GALF does not include woody crops or shifting cultivation, which may introduce regional biases in arable land extent. For example, our results diverge from earlier studies in Southeast Asia[14,62] that reported significant cropland expansion driven by the proliferation of woody crops like oil palm plantations. This is corroborated by FAO statistics in Indonesia, where total cropland (including woody crops) increased from 334,410 to 433,823 km^2, while arable land declined slightly from 179,410 to 177,987 km^2 between 2000 and 2020. Consequently, our findings may represent a conservative estimate, and the inclusion of woody crops may further reinforce the conclusion that cropland is increasingly redistributed toward tropical climates. Second, the GHSL-derived built-up dataset does not explicitly account for impervious surfaces, the difference between urban cores and rural settlements, and population density, which may limit its ability to fully capture the intensity of human settlement at local scales. Third, the climatic structuring of arable land and human settlements varies by continent. For example, arid steppe (BSh) and tropical savannah (Aw) regions are more extensively developed in South Asia than in Africa and South America. This divergence likely reflects historical and socioeconomic disparities —including population density, legacy infrastructure, and economic conditions—that warrant further investigation. Fourth, the proposed hypothesis primarily focuses on climate-scale arable land redistribution and is not intended to capture all drivers of land-use change, which are also shaped by a complex interplay of local socioeconomic[38], policy[39], and environmental factors[40–42,63]. For example, soil and site conditions may further influence where cultivation occurs within climatically suitable regions, although recent evidence suggests that hydrological conditions such as precipitation and groundwater can outweigh soil texture in shaping agricultural land use[63]. Lastly, the scarcity of long-term (≥20 years) time-series datasets for arable land and built-up areas represents a potential source of uncertainty in our findings. To assess the robustness of our findings, we replicated our analyses using the GLAD dataset[64], which yielded consistent results (Supplementary Discussion).

Despite these limitations, our findings suggest that strategies for reconciling agricultural production with settlement expansion should differ across land-use contexts. In regions where competition between built-up and arable land is already pronounced, protecting high-quality existing arable land and limiting avoidable settlement encroachment may help reduce further displacement[23]. In regions characterized by co-development, particularly where expansion occurs at the expense of natural landscapes, forward-looking land-use planning may help prevent a transition toward more intensive competition. Importantly, because arable-land loss in densely developed regions can be accompanied by agricultural expansion elsewhere, land-use planning should also consider displacement effects beyond local boundaries[22]. Expansion into tropical, dryland, highland, and other resource-constrained environments may transfer environmental costs to forests[6,36,37,55], biodiversity[2,17,50,56–58], water resources[19–21], and other natural systems[14]. Thus, the principal policy implication of our analysis is not a single global prescription, but the need to recognize the different stages of settlement–agriculture interaction and the potential for local land competition to generate geographically distant environmental pressures.

Methods

Global arable land mapping data

We constructed a 1-km GALF by integrating multiple global satellite-derived land cover products with long-term temporal coverage (≥20 years) and high to medium spatial resolution (≤500 m), selecting only those with consistent temporal characteristics and spatial continuity. The FROM-GLC product[65] was excluded due to variability in input scene timing that affected spatial coherence, while certain regional land cover products were also omitted to maintain consistency across regions. The included global products are the International Geosphere-Biosphere Programme (IGBP) from the Moderate Resolution Imaging Spectroradiometer (MODIS, MCD12Q1 v061)[66], European Space Agency's Climate Change Initiative (CCI)[67], GlobeLand30[68], Global Land Analysis and Discovery (GLAD) dataset[64], and GLC_FCS30D[69]. Detailed specifications on cropland definitions, spatial resolutions, and temporal coverages for each dataset are provided in Supplementary Table S3. Note that for datasets that do not explicitly distinguish arable land from permanent croplands, we hereinafter refer to all such areas collectively as cropland.

As shown in Supplementary Table S3 and discussed previously[31], cropland definitions vary across products and deviate from the FAO cropland definition, which includes both arable land and permanent crops. This introduces possible bias in our and similar analyses. For instance, three products (CCI, GlobeLand30, and GLC_FCS30D) include permanent crops, mostly woody tree crops (e.g., oil palm, cocoa, coffee, rubber, and orchards). Conversely, MODIS and GLAD cropland maps exclude them. Furthermore, it has been shown that the annual crops component of most products is in fact aligned more with the FAO definition of temporary crops rather than arable land, which includes components that are difficult to see from remote sensing[31,70].

Harmonizing global arable land datasets

To harmonize different products and enhance consistency with the FAO definition of arable land, we developed a synergy approach[71–76] for generating GALF, the workflow of which is illustrated in Supplementary Fig. S8. Unlike previous studies[71–76], we focused exclusively on arable land rather than including permanent crops for the following reasons: (1) arable land is more consistently represented across land cover products and FAO statistics (Supplementary Table S3), and (2) the harmonization and validation of GALF rely on ground reference samples[65,77–80] that are typically interpreted from satellite or aerial imagery, which could mix woody crops with forests due to their tree-like canopy structure and phenological characteristics. In other words, even if synergized cropland maps were generated following the FAO cropland definition (i.e., including both arable land and permanent crops), it would be difficult to reliably validate the permanent crop component.

In constructing GALF, the synergy approach integrates five land cover products with FAO country-level arable land use statistics (FAOSTAT)[81], considering only the arable land components for products that explicitly distinguish them from woody crops. Woody vegetation was further excluded using the GLAD tree cover mask[64]. The approach assumes that high agreement among input layers increases confidence in arable land presence (Supplementary Fig. S9), generally leading to improved mapping accuracy[72–76]. Given that most agreement scores can result from multiple combinations of land cover products (Supplementary Fig. S10), this method first requires ranking the performance of each individual product. Unlike previous studies that rely solely on expert judgment, ground reference samples, or FAOSTAT for ranking[72–76], our approach ranked the products based on both their accuracy against ground reference samples and their consistency with FAOSTAT. This is based on the assumption that the product with the highest accuracy against ground reference samples should also show the closest agreement with FAOSTAT country-level arable land area, provided that sufficient validation samples are available and the FAO statistics are reliable. Specifically, for each country, land cover products were first evaluated and ranked by their overall accuracy when at least 20 validation samples were available, considering some countries with small land areas. To avoid over-interpreting marginal differences, only two decimal places of overall accuracy were considered[74]. In cases where products had identical accuracy or fewer than 20 validation samples were available, the product whose arable land area was closest to the FAOSTAT was assigned a higher rank. In some regions lacking FAOSTAT, rankings were based on continental-scale validation results across nine continental regions (Supplementary Fig. S11), which were delineated according to administrative boundaries[82] and the spatial clustering patterns of global arable land (Fig. 1a). More information on ground samples and the performance evaluation of land cover products is provided in the section below.

Once country-level performance rankings of input land cover products were available, an agreement-ranking score lookup table was established based on binary permutations to prioritize high-ranked regions that best matched reference data (Supplementary Table S4). Different from previous research that converted binary permutations to either agreement scores[72–75] or binary scores[76], this study combined both scoring approaches to enhance the likelihood of identifying the optimal configuration that best aligns with ground validation samples and FAO statistics. This is because we found that each scoring method has inherent limitations, but they offer complementary strengths when used together. The agreement-score approach[72–75] prioritizes regions where multiple products consistently indicate the presence of arable land (Supplementary Fig. S10). This method is particularly effective in regions where the input land cover products have comparable accuracy; however, it may underperform in cases where one product significantly outperforms the others. For example, if a single product accurately captures the full extent of arable land, it may mistakenly prioritize regions where multiple lower-performing products indicate arable land over areas correctly identified by the high-performing product alone. Conversely, the binary-score approach[76] gives priority to regions identified by the best-performing product but may be less effective when multiple products exhibit similar accuracy (Supplementary Fig. S10). Thus, combining both approaches increases the diversity of scoring combinations and enhances the ability to identify the configuration that best matches ground validation samples and FAO statistics. In this study, applying the combined method to five input products resulted in a total of 58 unique scoring combinations, whereas using either approach alone yielded only 32 combinations (i.e., 2^5; see Supplementary Table S4).

Then, the ground samples and FAOSTAT were used again as benchmarks to identify the best-performing scoring combinations. We found that the combination yielding the highest overall accuracy did not always align with the one most closely matching the FAOSTAT-reported arable land area, particularly in African countries. This discrepancy is likely attributable to relatively low agreement among five land cover products over Africa (Supplementary Fig. S9) and the inherent uncertainties in both the ground reference and FAOSTAT data[83]. To balance both criteria, for countries with more than 20 validation samples, we retained only those combinations that either exceeded the overall accuracy of the best individual product or ranked within the top 10% of all combinations based on overall accuracy. Among these, the combination with the closest arable land area to the FAOSTAT was selected. For countries lacking sufficient validation samples, the FAOSTAT alone was used to select the best combination. In cases where FAOSTAT data were unavailable, but more than 20 validation samples were present, ground samples were directly used to identify the optimal combination. For regions lacking both adequate validation samples and FAOSTAT data, the best combination was selected based on the corresponding continental validation results.

Finally, the 1-km GALF was computed by averaging arable land weights at 100-m subpixels within areas defined by the optimal scoring combination through the Google Earth Engine[84]. Considering that the spatial resolution varies across input land cover datasets, all products were first reprojected into a common coordinate system (WGS84; EPSG:4326) and resampled to a 100-m resolution to facilitate the calculation of arable land fractions at the 1-km scale. In this calculation, 100-m pixels classified as pure arable land by all overlapping products were assigned a weight of 1, while pixels identified as mosaics (i.e., a mix of cropland and other land cover types) by any product were assigned lower weights to reflect their partial arable land composition. Specifically, for CCI, mosaic cropland classes were weighed as 0.75 when cropland fraction exceeded 50%, and 0.25 when it was below 50%. For MODIS, mosaic cropland comprising 40–60% cultivated land was assigned a value of 0.5. In cases where a 100-m pixel was simultaneously labeled as pure arable land and mosaic arable land by different products, the assigned weight was averaged accordingly. Notably, a few small islands were not represented in the continental mask[82], for which the arable land fraction was directly calculated based on the GLAD dataset[64] due to its similarity to the FAO arable land definition, high spatial resolution, and reliable accuracy, as discussed below. We implemented the procedure using data from 2010 to identify the optimal scoring combination, which was then applied to generate GALF for the years 2000, 2010, and 2020. These 3 years represent the intersection of temporal coverage across all products, with MODIS land cover from 2001 used as a proxy for 2000.

It should be noted that, although the proposed method is expected to produce credible arable land maps beyond the capabilities of individual land cover products, its performance strongly depends on the quality of the input datasets and may fail to capture arable land in regions where most products perform poorly. One notable example is greenhouse agriculture, which should ideally be detected by all land

cover products but exhibits distinct spectral reflectance compared with other arable land[85]. We found that the ability of the products to detect greenhouse infrastructures varies considerably. As examined, while small- to medium-sized greenhouse facilities, such as those in Michoacán, Mexico (19.9°N, 102.2°W), are generally captured by all products, only GlobeLand30 and CCI successfully detect the large-scale greenhouse infrastructures (>500 km^2) in Almería, Spain (36.7°N, 2.7°W)[86,87]. In contrast, other products misclassify these areas as impervious surfaces (GLC_FCS30D), wetlands (GLAD), or non-vegetated land (MODIS). Consequently, the proposed method cannot reliably capture these large-scale greenhouse areas in Spain. To address this issue, we explicitly identified these greenhouse areas across Spain by combining GlobeLand30 and CCI arable land layers with GLC_FCS30D impervious surfaces and GLAD wetlands across Spain, before calculating the 1-km arable land fraction. Supplementary Fig. S12 demonstrates that this combined approach effectively captures the greenhouse areas in southern Spain. On the other hand, in Africa and the Arabian Peninsula, the quality and agreement among the five input cropland products were sometimes very low (Supplementary Fig. S9). For example, GLC_FCS30D missed an entire scene in Sudan, while CCI misclassified several roads within the Congolian rainforests as cropland. Therefore, we carefully compared GALF with GLAD by evaluating their overall accuracy, area consistency with FAOSTAT statistics, and spatial patterns of arable land distribution. Based on the assessment, we replaced GALF with GLAD in the Republic of the Congo, Democratic Republic of the Congo, South Sudan, Sudan, Somalia, and Saudi Arabia, where GLAD demonstrated comparable accuracy to GALF but provided more realistic spatial patterns.

Validation of land cover products and GALF

To support the performance ranking of land cover products in 2010 and identify the best scoring combination, we compiled multiple sources of reference samples (Supplementary Fig. S13). The year 2010 was selected because it represents the midpoint of the study period and offers the most consistent availability of ground validation data. The reference samples included two datasets from Tsinghua University[65,77] and additional samples from the Geo-wiki crowdsourcing platform[78] and the U.S. Geological Survey's Land Change Monitoring, Assessment and Projection (LCMAP)[79]. The Tsinghua University datasets[65,77] were originally developed to support the creation and validation of their 30-m global land cover product (i.e., FROM-GLC), where cropland is defined as arable and tillage land with herbaceous and/or shrub crops—thus more than arable land. The first dataset[65] involves 36,352 globally distributed random samples, manually labeled by hundreds of students, researchers, and experts using Google Earth imagery in or around 2010. The second dataset[77] contains 38,664 global random sample units spanning the years 1986 to 2010, derived through interpretation of Landsat imagery[88], MODIS enhanced vegetation index (EVI)[89], and other high-resolution images via Google Earth. For this study, a total of 11,672 samples in 2010 were considered. The Geo-wiki dataset[78,90] records the dominant, secondary, and tertiary land cover types, with cropland defined as "cultivated and managed" or "mosaic of cultivated and managed/natural vegetation". In this study, locations falling into any of the three cropland-related categories were considered as reference. It comprises 151,942 globally distributed random samples derived from the visual interpretation of Google Earth imagery before 2012. A subset of 12,555 samples from 2010 was selected for analysis. The LCMAP reference dataset[58] defines cropland as areas used for the production of crops, including cultivated and uncultivated croplands, hay fields, orchards, vineyards, and pasturelands actively managed for crop production. It offers annual land cover labels for approximately 25000 random locations across the contiguous United States (CONUS) from 1984 to 2021 based on systematic interpretation of Landsat imagery and aerial photographs. A subset of 24,995 samples from 2010 was used in this study. To integrate the four sample sets and avoid conflicting validation results, samples located within the same 1-km pixel were merged, and those indicating different land cover types were excluded. A 1-km resolution was adopted to ensure consistency in comparisons among the various land cover products and the GALF. This resulted in a final dataset of 61,294 samples.

To validate the performance of different land cover products in generating the synergized product, 1-km arable land fraction maps were first generated by averaging values from the 100-m resolution layers, where any pixel with an arable land fraction greater than zero was designated as arable land[75]. To facilitate consistent ranking of product performance, a single error metric—overall accuracy (OA), i.e., the sum of true positives and true negatives divided by the total number of samples—was adopted following previous studies[72–75]. This metric was used because it captures overall agreement with reference data across all classes, providing a consistent and comparable basis for ranking products within a synergized framework. Moreover, OA is less sensitive to inconsistencies in class definitions across different land cover products compared to class-specific metrics. Continental and global validation results for the five land cover products were summarized in Supplementary Table S5, indicating that MODIS achieved the highest overall accuracy globally and across most continents, followed by GLAD, GlobeLand30, CCI, and GLC_FCS30D. However, despite its strong performance, MODIS cannot be used independently to derive 1-km arable land fractions due to its relatively coarse native resolution of 500 m. These performance rankings, along with country-level validation results and FAOSTAT, form the basis for ranking individual land cover products and identifying the optimal scoring combinations.

To independently assess the accuracy of the GALF maps, we conducted a multi-scale validation in 2020 and compared it against other land cover products. Specifically, we first assessed its spatial accuracy using an independent reference sample set[80] (Supplementary Fig. S13), which defines cropland as rainfed and irrigated croplands following the United Nations' Land Cover Classification rule[91]. This dataset integrates multiple data sources, including high-resolution imagery from Google Earth, vegetation cover, plant phenology, tree height, and terrain characteristics, and comprises 79,112 random samples. To avoid duplicate and conflicting assessment results, samples located within the same 1-km pixel were merged, while those indicating different land cover types were removed, leading to a final dataset of 79,001 samples.

When compared with other land cover products, Supplementary Table S6 shows that GALF exhibits strong performance comparable to MODIS on the global scale and across all continents, followed by GLAD, GlobeLand30, CCI, and GLC_FCS30D. At the continental level, GALF outperforms all other products in four out of nine regions, ranking second in four and third in one. Similar results are also observed across different Köppen–Geiger climate zones: GALF achieves the highest accuracy in 12 out of 26 zones, ranks second in 10 zones, and third in four (Supplementary Table S7).

Global Arable Land Fraction

Supplementary Fig. S14 provides an overview of GALF patterns depicted by the GALF maps for the years 2000, 2010, and 2020. As shown, arable land is predominantly concentrated in the Northern Hemisphere, particularly in North America, Europe, South Asia, and East Asia. By contrast, arable land is more sparsely distributed in low-latitude and Southern Hemisphere regions, including South America, Africa, Southeast Asia, and Oceania. Supplementary Fig. S15 compares country-level arable land area estimates from various land cover products against FAO-reported statistics. GALF achieves the highest correlation ($R = 0.993$) and the lowest root mean square error ($RMSE = 2.35 \times 10^4$ km^2), demonstrating relatively high accuracy in capturing national-scale arable land area. Compared to GLAD and

MODIS, GALF improves the correlation by more than 0.6% and reduces RMSE by over 29%. For global total arable land, GLAD (1.32×10^7 km^2), GALF (1.31×10^7 km^2), and MODIS (1.46×10^7 km^2) are closest to the FAO-reported total (1.38×10^7 km^2), while other products (i.e., CCI, GlobeLand30, and GLC_FCS30D) significantly overestimate the global arable land area by more than 0.75×10^7 km^2.

Built-up fraction

To quantify built-up dynamics and ensure the robustness of our results, we derived 1-km built-up fractions using two independent datasets: the built-up surface data from the GHSL project[32,92] and built-up land data from GLAD[64]. The GHSL-based built-up fractions were used for the main analyses, whereas the GLAD-based fractions were used to replicate the analyses for intercomparison (see Supplementary Discussion).

Developed by the European Commission's Joint Research Centre as part of the Copernicus Emergency Management Service, GHSL defines built-up surface as the gross building footprint area (including wall thickness) enclosed by the outer building walls. The dataset was generated using a symbolic machine learning–based supervised classification approach[93] applied to Sentinel-2 imagery[94], achieving a high Intersection-over-Union (IoU)[95] score of 0.92, placing it among the most accurate publicly available built-up datasets. The data are temporally interpolated or extrapolated in 5-year intervals, covering the period from 1975 to 2030. In this study, 1-km built-up surface data for the years 2000, 2010, and 2020 were extracted and converted into built-up fractions by dividing the built-up area within each grid cell by the cell's total area. These GHSL-derived built-up fractions were used in combination with GALF for all analyses presented in the main text.

We additionally used the 30-m built-up land data from GLAD[64]. This product defines built-up land as areas containing man-made surfaces—including infrastructure, commercial, and residential land uses—even if such surfaces do not dominate within the pixel. It was produced using a deep learning convolutional neural network algorithm[96] applied to Landsat imagery, with training data collected from OpenStreetMap (https://planet.osm.org; https://www.openstreetmap.org). While the overall accuracy was not reported, the user's accuracy ranged from 63.7 to 74.1% and the producer's accuracy from 39.1 to 59.6%. In this study, we computed 1-km built-up fractions by averaging the 30-m GLAD classifications within each 1-km grid cell. Given its relatively low classification accuracy, this dataset was used solely to replicate the results presented in the main text (see Supplementary Discussion).

Climate classification

To understand the climatic constraints on arable land and built-up systems, we used the 1-km constant Köppen–Geiger climate classification map[33,97] for the period 1991–2020. The Köppen–Geiger system delineates five major climate zones—tropical (A), arid (B), temperate (C), cold (D), and polar (E)—based on seasonal patterns of monthly temperature and precipitation. Precipitation regimes are further classified as desert (W), steppe (S), fully humid (f), summer dry (s), winter dry (w), and monsoon (m), while temperature regimes include hot (h), cold (k), hot summer (a), warm summer (b), cold summer (c), cold winter (d), tundra (T), and frost (F). This classification scheme has been widely adopted in previously developed Köppen–Geiger climate classification maps[98,99]. Compared with earlier versions that have relatively coarse resolutions (≥0.1°), the product used in this study offers a higher spatial resolution (1 km) and includes corrections for topographic effects. It should be noted that although climate zones shift with rising global temperatures[33,100], they are expected to remain relatively stable over a few decades, as also evidenced by the relatively constant map for the period 1991–2020[33,97].

Historical land cover dynamics

To investigate the historical co-evolution of arable land and built-up areas, we used two long-term land cover reconstructions: the History Database of the Global Environment (HYDE v3.4)[34] and the Land-use Harmonization 2 (LUH2)[101]. HYDE3.4 provides spatially explicit reconstructions of cropland and built-up areas at a resolution of 5 arc minutes. It integrates historical census data, archeological records, and satellite observations to generate long-term time series from 10,000 BCE to 2024. Its most recent spatial allocation of land use is primarily informed by FAO agricultural land use data and the CCI land cover, supplemented with MODIS imagery and MapBiomas statistics (https://mapbiomas.org/) for Brazil, Indonesia, and China. The historical spatial allocation of built-up areas is estimated by dividing each country's total urban population by its average urban population density, while the allocation of cropland is determined as the residual area after accounting for water bodies, snow and ice, built-up areas, protected lands, and unused regions, which are calibrated using recent land cover products. In this study, we used data from 0 CE onwards. LUH2 offers global annual land-use states from 850 to 2100 at 0.25° resolution, combining historical reconstructions with future projections from integrated assessment models. Designed for Earth system modeling, LUH2 supports CMIP6 by providing consistent trajectories of land-use change, including cropland, pasture, forestry, and urban areas. Its historical land use is based on HYDE v3.2. In this work, we used historical LUH2 data from 850 to 2015. Note that although the definitions of cropland and built-up areas in these datasets differ from those in GALF and GHSL, we expect their historical evolution patterns to be largely consistent at climatic scales.

Data availability

The GALF data generated in this study are available at https://doi.org/10.5281/zenodo.17343790[102]. MODIS MCD12Q1 data are available at https://doi.org/10.5067/MODIS/MCD12Q1.061. ESA CCI data are available at https://maps.elie.ucl.ac.be/CCI/viewer/index.php. GlobeLand30 data are available at https://cloudcenter.tianditu.gov.cn/landCover. GLAD data are available at https://glad.umd.edu/dataset/GLCLUC2020. GLC_FCS30D data are available at https://doi.org/10.5281/zenodo.8239305. Historical land cover reconstructions are available from HYDE v3.4 (https://doi.org/10.24416/UU01-BV65K3) and LUH2 (https://luh.umd.edu). FAO arable land statistics are available at https://www.fao.org/faostat/en/#home. Ground validation samples were obtained from Tsinghua University (https://data-starcloud.pcl.ac.cn/iearthdata), Geo-Wiki (https://www.geo-wiki.org/), the USGS, and the Chinese Academy of Sciences (https://doi.org/10.5281/zenodo.7846090). GHSL built-up fraction data are accessed at https://human-settlement.emergency.copernicus.eu/datasets.php. The Köppen–Geiger climate classification map is available at https://www.gloh2o.org/koppen. All datasets are also available on request from L.G.

Code availability

The major codes used to analyze the data, reproduce the results, and create the main figures are available and reproducible at https://doi.org/10.5281/zenodo.20059382.

References

1. Foley, J. A. et al. Global consequences of land use. *Science* **309**, 570–574 (2005).
2. Ramankutty, N. & Foley, J. A. Estimating historical changes in global land cover: croplands from 1700 to 1992. *Glob. Biogeochem. Cycles* **13**, 997–1027 (1999).
3. Luyssaert, S. et al. Land management and land-cover change have impacts of similar magnitude on surface temperature. *Nat. Clim. Change* **4**, 389–393 (2014).
4. FAO. *Land Statistics 2001–2023—Global, Regional and Country Trends*. https://doi.org/10.4060/cd5765en (FAO, 2025).

5. United Nations Department of Economic and Social Affairs, Population Division. *World Population Prospects: The 2017 Revision—Data Booklet*. (United Nations Department of Economic and Social Affairs, Population Division, 2017).
6. Foley, J. A. et al. Solutions for a cultivated planet. *Nature* **478**, 337–342 (2011).
7. Godfray, H. C. J. et al. Food security: the challenge of feeding 9 billion people. *Science* **327**, 812–818 (2010).
8. Tilman, D., Balzer, C., Hill, J. & Befort, B. L. Global food demand and the sustainable intensification of agriculture. *Proc. Natl. Acad. Sci. USA* **108**, 20260–20264 (2011).
9. Crist, E., Mora, C. & Engelman, R. The interaction of human population, food production, and biodiversity protection. *Science* **356**, 260–264 (2017).
10. Potapov, P. et al. Global maps of cropland extent and change show accelerated cropland expansion in the twenty-first century. *Nat. Food* **3**, 19–28 (2022).
11. Winkler, K., Fuchs, R., Rounsevell, M. & Herold, M. Global land use changes are four times greater than previously estimated. *Nat. Commun.* **12**, 2501 (2021).
12. Molotoks, A. et al. Global projections of future cropland expansion to 2050 and direct impacts on biodiversity and carbon storage. *Glob. Change Biol.* **24**, 5895–5908 (2018).
13. Gibbs, H. K. et al. Tropical forests were the primary sources of new agricultural land in the 1980s and 1990s. *Proc. Natl. Acad. Sci. USA* **107**, 16732–16737 (2010).
14. Zeng, Z. et al. Highland cropland expansion and forest loss in Southeast Asia in the twenty-first century. *Nat. Geosci.* **11**, 556–562 (2018).
15. Davis, K. F. et al. Tropical forest loss enhanced by large-scale land acquisitions. *Nat. Geosci.* **13**, 482–488 (2020).
16. Song, X.-P. et al. Massive soybean expansion in South America since 2000 and implications for conservation. *Nat. Sustain.* **4**, 784–792 (2021).
17. Pendrill, F. et al. Disentangling the numbers behind agriculture-driven tropical deforestation. *Science* **377**, eabm9267 (2022).
18. Schneider, J. M. et al. Effects of profit-driven cropland expansion and conservation policies. *Nat. Sustain.* **7**, 1335–1347 (2024).
19. Gleeson, T., Wada, Y., Bierkens, M. F. & Van Beek, L. P. Water balance of global aquifers revealed by groundwater footprint. *Nature* **488**, 197–200 (2012).
20. Jasechko, S. et al. Rapid groundwater decline and some cases of recovery in aquifers globally. *Nature* **625**, 715–721 (2024).
21. Mishra, V., Solanki, H. & Nemani, R. Greening of the Thar Desert driven by climate change and human interventions. *Cell Rep. Sustain.* **2**, 100364 (2025).
22. van Vliet, J. Direct and indirect loss of natural area from urban expansion. *Nat. Sustain.* **2**, 755–763 (2019).
23. Bren d'Amour, C. et al. Future urban land expansion and implications for global croplands. *Proc. Natl. Acad. Sci. USA* **114**, 8939–8944 (2017).
24. Chen, G. et al. Global projections of future urban land expansion under shared socioeconomic pathways. *Nat. Commun.* **11**, 537 (2020).
25. Seto, K. C., Güneralp, B. & Hutyra, L. R. Global forecasts of urban expansion to 2030 and direct impacts on biodiversity and carbon pools. *Proc. Natl. Acad. Sci. USA* **109**, 16083–16088 (2012).
26. Newbold, T. et al. Global effects of land use on local terrestrial biodiversity. *Nature* **520**, 45–50 (2015).
27. Pereira, H. M. et al. Global trends and scenarios for terrestrial biodiversity and ecosystem services from 1900 to 2050. *Science* **384**, 458–465 (2024).
28. Li, L., Awada, T., Zhang, Y. & Paustian, K. Global land use change and its impact on greenhouse gas emissions. *Glob. Change Biol.* **30**, e17604 (2024).
29. Andela, N. et al. A human-driven decline in global burned area. *Science* **356**, 1356–1362 (2017).
30. FAO. *World Programme for the Census of Agriculture 2020. Volume I: Programme, Concepts and Definitions*. (FAO, 2017).
31. Tubiello, F. N. et al. Measuring the world's cropland area. *Nat. Food* **4**, 30–32 (2023).
32. Pesaresi, M. et al. Advances on the Global Human Settlement Layer by joint assessment of Earth Observation and population survey data. *Int. J. Digit. Earth* **17**, 2390454 (2024).
33. Beck, H. E. et al. High-resolution (1 km) Köppen-Geiger maps for 1901–2099 based on constrained CMIP6 projections. *Sci. Data* **10**, 724 (2023).
34. Klein Goldewijk, K., Beusen, A., Doelman, J. & Stehfest, E. Anthropogenic land use estimates for the Holocene—HYDE 3.2. *Earth Syst. Sci. Data* **9**, 927–953 (2017).
35. Keenleyside, C., Tucker, G. & McConville, A. *Farmland Abandonment in the EU: An Assessment of Trends and Prospects*. (Institute for European Environmental Policy, 2010).
36. Ren, C. et al. Ageing threatens sustainability of smallholder farming in China. *Nature* **616**, 96–103 (2023).
37. Wright, C. K. & Wimberly, M. C. Recent land use change in the Western Corn Belt threatens grasslands and wetlands. *Proc. Natl. Acad. Sci. USA* **110**, 4134–4139 (2013).
38. Prishchepov, A. V., Radeloff, V. C., Baumann, M., Kuemmerle, T. & Müller, D. Effects of institutional changes on land use: agricultural land abandonment during the transition from state-command to market-driven economies in post-Soviet Eastern Europe. *Environ. Res. Lett.* **7**, 024021 (2012).
39. Hua, F. et al. Opportunities for biodiversity gains under the world's largest reforestation programme. *Nat. Commun.* **7**, 12717 (2016).
40. Amiri, A., Ebtehaj, I., Soltani, K., Gumiere, S. J. & Bonakdari, H. Future soil erosion trends in Canadian agricultural lands from runoff and sustainability impacts. *Sci. Rep.* **15**, 23184 (2025).
41. You, N. et al. Climate-driven global cropland changes and consequent feedbacks. *Nat. Geosci.* **18**, 639–645 (2025).
42. Sloat, L. L. et al. Climate adaptation by crop migration. *Nat. Commun.* **11**, 1243 (2020).
43. Wang, S. et al. Urbanization can benefit agricultural production with large-scale farming in China. *Nat. Food* **2**, 183–191 (2021).
44. Sumner, D. A. & Zulauf, C. *Economic & Environmental Effects of Agricultural Insurance Programs*. (Council on Food, Agricultural, and Resource Economics (C-FARE), 2012).
45. Chen, W., Yuan, Y., Gu, T., Ma, H. & Zeng, J. What factors drove the global cropland expansion into highlands? *Earth's Future* **13**, e2024EF005337 (2025).
46. Mountain Research Initiative EDW Working Group Elevation-dependent warming in mountain regions of the world. *Nat. Clim. Change* **5**, 424–430 (2015).
47. Lambin, E. F. & Meyfroidt, P. Global land use change, economic globalization, and the looming land scarcity. *Proc. Natl. Acad. Sci. USA* **108**, 3465–3472 (2011).
48. Liu, J. et al. Framing sustainability in a telecoupled world. *Ecol. Soc.* **18** (2013).
49. Yu, Y., Feng, K. & Hubacek, K. Tele-connecting local consumption to global land use. *Glob. Environ. Change* **23**, 1178–1186 (2013).
50. Kastner, T., Rivas, M., Koch, W. & Nonhebel, S. Global changes in diets and the consequences for land requirements for food. *Proc. Natl. Acad. Sci. USA* **109**, 6868–6872 (2012).
51. Borras, S. M., Kay, C., Gómez, S. & Wilkinson, J. Land grabbing and global capitalist accumulation: key features in Latin America. *Can. J. Dev. Stud. Rev. can. détudes du dév.* **33**, 402–416 (2012).
52. Cotula, L., Vermeulen, S., Leonard, R. & Keeley, J. *Land Grab or Development Opportunity? Agricultural Investment and International Land Deals in Africa*. (IIED, 2009).

53. Mueller, N. D. et al. Closing yield gaps through nutrient and water management. *Nature* **490**, 254–257 (2012).
54. Duan, J. et al. Consolidation of agricultural land can contribute to agricultural sustainability in China. *Nat. Food* **2**, 1014–1022 (2021).
55. Krausmann, F. et al. Global human appropriation of net primary production doubled in the 20th century. *Proc. Natl. Acad. Sci. USA* **110**, 10324–10329 (2013).
56. Phalan, B., Onial, M., Balmford, A. & Green, R. E. Reconciling food production and biodiversity conservation: land sharing and land sparing compared. *Science* **333**, 1289–1291 (2011).
57. Kremen, C. Reframing the land-sparing/land-sharing debate for biodiversity conservation. *Ann. N. Y. Acad. Sci.* **1355**, 52–76 (2015).
58. Sietz, D. et al. Mapping human-nature archetypes to guide global biodiversity, food security, and land-use policy. *One Earth* **8**, 101416 (2025).
59. Brabec, E. & Smith, C. Agricultural land fragmentation: the spatial effects of three land protection strategies in the eastern United States. *Landsc. Urban Plan.* **58**, 255–268 (2002).
60. Lichtenberg, E. & Ding, C. Assessing farmland protection policy in China. *Land Use Policy* **25**, 59–68 (2008).
61. Cammelli, F. et al. Deforestation-focused policies do not reduce degradation in the Brazilian Amazon. *Proc. Natl. Acad. Sci. USA* **123**, e2507793123 (2026).
62. Gao, X. et al. The importance of distinguishing between natural and managed tree cover gains in the moist tropics. *Nat. Commun.* **16**, 6092 (2025).
63. Emde, D., Don, A., Mueller, C. W. & Schneider, F. Hydrological conditions outweigh soil texture, temperature, and terrain in German agricultural land use. *J. Plant Nutr. Soil Sci.* **189**, 243–254 (2026).
64. Potapov, P. et al. The Global 2000-2020 Land Cover and Land Use Change Dataset derived from the Landsat Archive: first results. *Front. Remote Sens.* **3**, 856903 (2022).
65. Gong, P. et al. Finer resolution observation and monitoring of global land cover: first mapping results with Landsat TM and ETM+ data. *Int. J. Remote Sens.* **34**, 2607–2654 (2013).
66. Friedl, M. A. et al. Global land cover mapping from MODIS: algorithms and early results. *Remote Sens. Environ.* **83**, 287–302 (2002).
67. European Space Agency. *Climate Change Initiative Land Cover*. (European Space Agency, 2015).
68. Chen, J. et al. Global land cover mapping at 30m resolution: a POK-based operational approach. *ISPRS J. Photogramm. Remote Sens.* **103**, 7–27 (2015).
69. Zhang, X. et al. GLC_FCS30D: the first global 30 m land-cover dynamics monitoring product with a fine classification system for the period from 1985 to 2022 generated using dense-time-series Landsat imagery and the continuous change-detection method. *Earth Syst. Sci. Data* **16**, 1353–1381 (2024).
70. Kerr, J. T. & Cihlar, J. Land use and cover with intensity of agriculture for Canada from satellite and census data. *Glob. Ecol. Biogeogr.* **12**, 161–172 (2003).
71. Jung, M., Henkel, K., Herold, M. & Churkina, G. Exploiting synergies of global land cover products for carbon cycle modeling. *Remote Sens. Environ.* **101**, 534–553 (2006).
72. Ramankutty, N., Evan, A. T., Monfreda, C. & Foley, J. A. Farming the planet: 1. Geographic distribution of global agricultural lands in the year 2000. *Glob. Biogeochem. Cycles* **22** (2008).
73. Fritz, S. et al. Cropland for sub-Saharan Africa: a synergistic approach using five land cover data sets. *Geophys. Res. Lett.* **38** (2011).
74. Fritz, S. et al. Mapping global cropland and field size. *Glob. Change Biol.* **21**, 1980–1992 (2015).
75. Lu, M. et al. A cultivated planet in 2010: 1. The global synergy cropland map. *Earth Syst. Sci. Data Discuss.* **2020**, 1–33 (2020).
76. Tubiello, F. N. et al. A new cropland area database by country circa 2020. *Earth Syst. Sci. Data* **15**, 4997–5015 (2023).
77. Zhao, Y. et al. Towards a common validation sample set for global land-cover mapping. *Int. J. Remote Sens.* **35**, 4795–4814 (2014).
78. Fritz, S. et al. A global dataset of crowdsourced land cover and land use reference data. *Sci. Data* **4**, 1–8 (2017).
79. Stehman, S. V., Pengra, B. W., Horton, J. A. & Wellington, D. F. Validation of the US Geological Survey's Land Change Monitoring, Assessment and Projection (LCMAP) collection 1.0 annual land cover products 1985–2017. *Remote Sens. Environ.* **265**, 112646 (2021).
80. Zhao, T. et al. Assessing the accuracy and consistency of six fine-resolution global land cover products using a novel stratified random sampling validation dataset. *Remote Sens* **15**, 2285 (2023).
81. FAO. FAOSTAT land use. (2019).
82. U.S. Department of State, Office of the Geographer. Large Scale International Boundaries (LSIB)—Simplified. (2017).
83. The World Bank. *Global Strategy to Improve Agricultural and Rural Statistics*. https://www.fao.org/fileadmin/templates/ess/documents/meetings_and_workshops/ICAS5/Ag_Statistics_Strategy_Final.pdf (The World Bank, 2011).
84. Gorelick, N. et al. Google Earth Engine: planetary-scale geospatial analysis for everyone. *Remote Sens. Environ.* **202**, 18–27 (2017).
85. Tong, X. et al. Global area boom for greenhouse cultivation revealed by satellite mapping. *Nat. Food* **5**, 513–523 (2024).
86. Gómez-Galán, M., Pérez-Alonso, J., Callejón-Ferre, Á-J. & Sánchez-Hermosilla-López, J. Assessment of postural load during melon cultivation in Mediterranean greenhouses. *Sustainability* **10**, 2729 (2018).
87. Mendoza-Fernández, A. J., Peña-Fernández, A., Molina, L. & Aguilera, P. A. The role of technology in greenhouse agriculture: Towards a sustainable intensification in Campo de Dalías (Almería, Spain). *Agronomy* **11**, 101 (2021).
88. Woodcock, C. E. et al. Free access to Landsat imagery. *Science* **320**, 1011 (2008).
89. Huete, A. et al. Overview of the radiometric and biophysical performance of the MODIS vegetation indices. *Remote Sens. Environ.* **83**, 195–213 (2002).
90. Anderson, J. R. *A Land Use and Land Cover Classification System for Use with Remote Sensor Data*. Vol. 964 (US Government Printing Office, 1976).
91. Di Gregorio, A. *Land Cover Classification System: Classification Concepts and User Manual: LCCS*. Vol. 8 (Food and Agriculture Organization of the United Nations (FAO), 2005).
92. European Commission: Joint Research Centre. *GHSL Data Package 2023*. https://data.europa.eu/doi/10.2760/098587 (European Commission: Joint Research Centre, 2023).
93. Garnelo, M. & Shanahan, M. Reconciling deep learning with symbolic artificial intelligence: representing objects and relations. *Curr. Opin. Behav. Sci.* **29**, 17–23 (2019).
94. Phiri, D. et al. Sentinel-2 data for land cover/use mapping: a review. *Remote Sens* **12**, 2291 (2020).
95. Everingham, M., Van Gool, L., Williams, C. K. I., Winn, J. & Zisserman, A. The Pascal Visual Object Classes (VOC) challenge. *Int. J. Comput. Vis.* **88**, 303–338 (2010).
96. Ronneberger, O., Fischer, P. & Brox, T. U-Net: convolutional networks for biomedical image segmentation. in *Medical Image Computing and Computer-Assisted Intervention – MICCAI 2015* Vol. 9351 (eds Navab, N., Hornegger, J., Wells, W. M. & Frangi, A. F.) 234–241 (Springer International Publishing, 2015).
97. Beck, H. E. et al. Present and future Köppen-Geiger climate classification maps at 1-km resolution. *Sci. Data* **5**, 180214 (2018).

98. Kottek, M., Grieser, J., Beck, C., Rudolf, B. & Rubel, F. World Map of the Köppen-Geiger climate classification updated. *Meteorol. Z.* **15**, 259–263 (2006).
99. Peel, M. C., Finlayson, B. L. & McMahon, T. A. Updated world map of the Köppen-Geiger climate classification. *Hydrol. Earth Syst. Sci.* **11**, 1633–1644 (2007).
100. Mahlstein, I., Daniel, J. S. & Solomon, S. Pace of shifts in climate regions increases with global temperature. *Nat. Clim. Change* **3**, 739–743 (2013).
101. Hurtt, G. C. et al. Harmonization of global land use change and management for the period 850–2100 (LUH2) for CMIP6. *Geosci. Model Dev.* **13**, 5425–5464 (2020).
102. Gao, L. et al. 1-km Global Arable Land Fraction (GALF) in 2000, 2010, and 2020. (2025).

Acknowledgements

L.G. thanks Dr. Liangyun Liu (Chinese Academy of Sciences), Dr. Le Yu (Tsinghua University), Dr. Miao Lu (Chinese Academy of Agricultural Sciences), Dr. Hankui Zhang (South Dakota State University), Dr. Maria Antonia Brovelli (Politecnico di Milano), Dr. Hao Wu (National Geomatics Center of China), and Ms. Xiaoqing Xu (Pengcheng Laboratory) for their assistance in acquiring land cover products and ground validation samples. The conclusions expressed in this paper are the authors' only and do not represent the views and policy of FAO on the subject matter.

Author contributions

Conceptualization: L.G. Data curation: L.G. Visualization: L.G. Writing—original draft: L.G. Project administration: D.R. Funding acquisition: D.R. Investigation: L.G., D.R., X.L., W.A., C.L., E.M., F.S., P.P., F.T., S.F., J.M., and L.Y. Writing—review and editing: L.G., D.R. X.L., W.A., C.L. E.M., F.S., P.P., F.T., S.F., J.M. and L.Y.

Funding

L.G. and D.R. disclose support for the research of this work from the World Resources Institute (WRI) [grant number G3275], U.S. Geological Survey (USGS) [grant number G24AC00247-00], U.S. Forest Service [grant number 24-JV-11242305-097], and the Institute on the Environment at the University of Minnesota. X.L. and J.M. disclose support from the Department of Energy Office of Science [grant number DE-AC05-00OR22725]. C.L. receives support from the Natural Sciences and Engineering Research Council of Canada [Discovery Grant RGPIN-2026-06521].

Competing interests

The authors declare no competing interests.

Additional information

Supplementary information The online version contains supplementary material available at https://doi.org/10.1038/s41467-026-79126-z.

Correspondence and requests for materials should be addressed to Lun Gao.

Peer review information *Nature Communications* thanks the anonymous reviewers for their contribution to the peer review of this work. A peer review file is available.

Reprints and permissions information is available at http://www.nature.com/reprints

Publisher's note Springer Nature remains neutral with regard to jurisdictional claims in published maps and institutional affiliations.

Open Access This article is licensed under a Creative Commons Attribution-NonCommercial-NoDerivatives 4.0 International License, which permits any non-commercial use, sharing, distribution and reproduction in any medium or format, as long as you give appropriate credit to the original author(s) and the source, provide a link to the Creative Commons licence, and indicate if you modified the licensed material. You do not have permission under this licence to share adapted material derived from this article or parts of it. The images or other third party material in this article are included in the article's Creative Commons licence, unless indicated otherwise in a credit line to the material. If material is not included in the article's Creative Commons licence and your intended use is not permitted by statutory regulation or exceeds the permitted use, you will need to obtain permission directly from the copyright holder. To view a copy of this licence, visit http://creativecommons.org/licenses/by-nc-nd/4.0/.

© The Author(s) 2026

This Article in Press is shared early to give you faster access to new research. It is citable and carries a permanent DOI. The final edited version will replace it automatically.

[1]Institute on the Environment, University of Minnesota, St. Paul, MN, USA. [2]Environmental Sciences Division, Oak Ridge National Laboratory, Oak Ridge, TN, USA. [3]Earth System Science Interdisciplinary Center, University of Maryland, College Park, MD, USA. [4]Earth Science Division, NASA Goddard Space Flight Center, Greenbelt, MD, USA. [5]Geographical Sciences, University of Maryland, College Park, MD, USA. [6]Department of Earth and Atmospheric Science, University of Quebec in Montreal, Montreal, QC, Canada. [7]Department of Geography, Dartmouth College, Hanover, NH, USA. [8]Neukom Institute for Computational Science, Dartmouth College, Hanover, NH, USA. [9]World Resources Institute, Washington, DC, USA. [10]Statistics Division, Food and Agriculture Organization of the United Nations, Rome, Italy. [11]International Institute for Applied Systems Analysis (IIASA), Laxenburg, Austria. [12]International Food Policy Research Institute, Washington, DC, USA. [13]Digital Agricultural Research Institute, College of Economics and Management, Huazhong Agricultural University, Wuhan, China. ✉e-mail: gaoxx996@umn.edu